EurJIC
European Journal of Inorganic Chemistry

Full Paper
doi.org/10.1002/ejic.202000243

Chemistry Europe
European Chemical Societies Publishing

Fused Metalloporphyrins | *Very Important Paper* |

VIP

Constitution and Conductivity of Metalloporphyrin Tapes

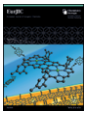

Giuseppe Bengasi,[a,b] Louise Quétu,[a] Kamal Baba,[a] Alexander Ost,[a] João P. Cosas Fernandes,[a] Patrick Grysan,[a] Katja Heinze,*[b] and Nicolas D. Boscher*[a]

Abstract: Metalloporphyrin tapes form in a solvent-free oxidative chemical vapor deposition process on glass substrates. The metal center (M = Ni^{II}, Cu^{II}, Zn^{II}, Co^{II}, Pd^{II}, $Fe^{III}Cl$, 2H) in the 5,15-disubstituted porphyrin monomer affects the initial C–C coupling step and consequently the formation of triply or doubly linked porphyrin tapes as well as the interchain interaction in the tape as shown by optical spectroscopy, high resolution mass spectrometry and X-ray photoelectron spectroscopy. Optical spectroscopy and conductive atomic force microscopy reveal that these factors influence the near-infrared absorbance and the electrical conductivity of the films. Consequently, the metal ion of the metalloporphyrin allows tuning of the macroscopic properties of the thin films composed of metalloporphyrin tapes.

Introduction

Porphyrin polymers and especially porphyrin tapes (Scheme 1) are promising materials for applications as near-infrared absorbers,[1] in non linear optics[2,3] and as molecular wires and electrodes.[4,5] However, their integration in optoelectronic devices is often hindered by their tedious multistep synthesis and poor solubility. The synthesis of porphyrin dimers, oligomers and porphyrin tapes relies on the oxidative coupling of porphyrins with free β and *meso* positions. This can lead to the formation of doubly or triply linked porphyrins in solution-based syntheses (Scheme 1). In solution-based oxidative C–C coupling reactions, the regioselectivity towards doubly or triply-linked porphyrin tapes (Scheme 1) depends on the porphyrin metal center.[6–8] Up to date, oligomeric directly fused porphyrins with Zn^{II},[1] Ni^{II},[7,9] Pd^{II}[6,7,10] or Cu^{II}[7,11,12] as central metal ions prepared via solution-based approaches have been reported. Zinc(II) porphyrins yield triply-linked porphyrin tapes with high regioselectivity. Such triply linked tapes exhibit highly interesting properties for optoelectronic device fabrication.[1,4,13] Other cations preferably form doubly-linked (β-*meso*, *meso*-β) or mixed porphyrin tapes with lower regioselectivity. Consequently, the careful selection of the metal cation provides a straightforward pathway for tuning the porphyrin tapes' optical, electronic and potential catalytic properties.[14–18] The synthesis of triply-linked zinc(II) porphyrin tapes is usually achieved in a two-step reaction. First, a *meso-meso* connection forms between porphyrin units employing Ag^+ oxidants.[19] Subsequently, a second dehydrogenation step delivers triply-linked porphyrin tapes.[1] During the last two decades, a significant effort has been devoted to develop an efficient synthetic access of multiply-linked porphyrin tapes in a single step by varying porphyrin, oxidant and solvent.[7,9,11,12,20–22] A single-step synthesis of doubly-linked porphyrins in solution has been successfully achieved,[7,9] yet the direct synthesis of triply-linked porphyrin tapes remains elusive up-to date.

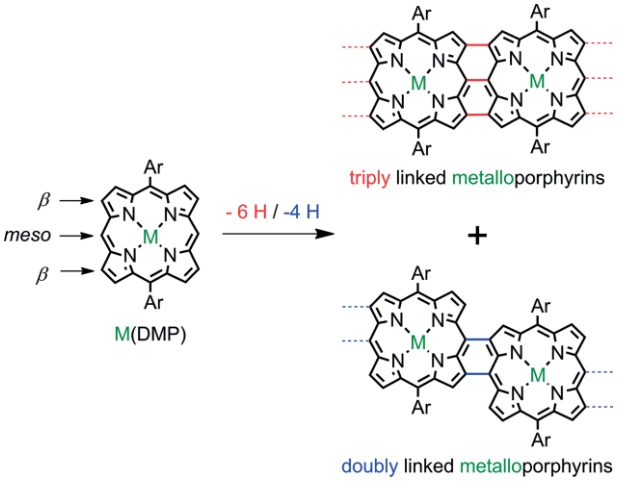

Scheme 1. Triply (red bonds) or doubly linked (blue bonds) metalloporphyrin tapes or mixed linkages in a polymer chain formed by dehydrogenative coupling of 5,15-diaryl metalloporphyrins.

The gas phase reaction of nickel(II) porphyrins and iron(III) chloride as oxidant delivers nickel porphyrin tapes directly in a

[a] *G. Bengasi, L. Quétu, Dr. K. Baba, A. Ost, Dr. J. P. Cosas Fernandes, P. Grysan, Dr. N. D. Boscher*
Materials Research and Technology, Luxembourg Institute of Science and Technology (LIST),
5 Avenue des Hauts-Fourneaux, 4362 Esch/Alzette, Luxembourg
E-mail: nicolas.boscher@list.lu
https://www.list.lu/en/mrt
[b] *G. Bengasi, Prof. Dr. K. Heinze*
Department of Chemistry,
Johannes Gutenberg University of Mainz,
Duesbergweg 10-14, 55128 Mainz, Germany
E-mail: katja.heinze@uni-mainz.de
https://www.ak-heinze.chemie.uni-mainz.de
Supporting information and ORCID(s) from the author(s) for this article are available on the WWW under https://doi.org/10.1002/ejic.202000243.

Full Paper
doi.org/10.1002/ejic.202000243

single step.[23] In contrast to on-substrate syntheses yielding merely sub-monolayers,[24–27] oxidative chemical vapor deposition (oCVD)[28] directly deposits thin smooth layers on virtually any substrate of sufficient temperature stability (≈ 100 °C).[23,29] The oCVD approach circumvents the need for long alkyl substituents on the porphyrin which are required for a sufficient solubility in solution-based methods. Indeed, by operating from the gas phase, the oCVD process of porphyrins is compatible with various substituents, including small, sterically undemanding substituents. Reducing the substituent size decreases the intermolecular distances, improves the interchain π–π stacking and thus facilitates interchain electron transfer in the film.[30] Moreover, phenyl substituents with free *ortho* positions, allow dehydrogenative C–C coupling of the phenyl ring with the macrocycle during the oCVD process.[22,31] This intramolecular cyclization forces co-planarity between the phenyl substituent and the porphyrin macrocycle. This additional reactivity increases the size of the planar chromophore, favors the π–π interchain interaction and consequently improves the conductivity of the porphyrin tapes thin film.

As only nickel(II) porphyrins have been studied in oCVD up to date, the effects of the coordinated metal cation on the oxidative polymerization chemistry of metalloporphyrins and the properties of the porphyrin tapes thin film obtained by oCVD are unexplored. In order to investigate the influence of the metal center on the reactivity of porphyrins in oCVD and to eventually tune the properties of the resulting tapes, we study the oCVD reaction of metallo-5,15-(dimesityl)porphyrins M(DMP) with M = 2H, $Fe^{III}Cl$, Co^{II}, Ni^{II}, Cu^{II}, Zn^{II} and Pd^{II} with iron(III) chloride[22,28,32] as volatile and competent oxidant.

To prevent the intramolecular cyclization as side reaction,[30,31] which would interfere with the mass spectrometric analysis of the double or triple intermolecular dehydrogenative coupling reaction by forming isobaric species, *meso*-mesityl substituents with blocked *ortho* positions were employed in the metalloporphyrin monomers.

First, we report the thermal stability, the optimum temperatures for the individual oCVD processes and the redox properties of the employed metalloporphyrin monomers M(DMP). The morphology, composition, connectivity, optical properties and electrical conductivity of the obtained thin films are then elucidated by helium ion microscopy (HIM), X-ray photoelectron spectroscopy (XPS), laser desorption ionization high resolution mass spectrometry (LDI-HRMS), UV/Vis/NIR spectroscopy and conductive atomic force microscopy (C-AFM). A correlation of the metal center with the resulting film properties is finally developed and discussed.

Results and Discussion

Monomer Characterization

The thermal stability of the free-base and metallated 5,15-(dimesityl)porphyrins was studied by thermogravimetric analysis (TGA). All investigated porphyrins are thermally stable up to ca. 350 °C, confirming their suitability for the oCVD process (Supporting Information, Figure S1). Interestingly, different metal cations in the porphyrin core affect the sublimation temperature. Prior experiments determined the sublimation temperature (from 220 °C to 260 °C) of each individual porphyrin in order to sublime similar amounts of material and maintain the porphyrin/oxidant ratio as constant as possible (Supporting Information, Table S1). Following, the M(DMP)/$[M(DMP)]^{\cdot+}$ redox potential $E_{1/2}$ of all porphyrin monomers was determined by cyclic voltammetry in CH_2Cl_2 employing $[n Bu_4N][PF_6]$ as supporting electrolyte (Table 1; Supporting Information, Figure S2), i.e. with a weakly coordinating solvent and counterion to approximate the gas phase conditions in the oCVD process.

Table 1. Oxidation potentials of the porphyrin monomers (vs. FcH/FcH^+ in CH_2Cl_2 employing $[n Bu_4N][PF_6]$ as supporting electrolyte), thickness *d* and arithmetic average roughness *Ra* of the oCVD films.

Porphyrin	$E_{1/2}$ /V	Film thickness *d* /nm	Film roughness *Ra* /nm
FeCl(DMP)	0.62	38 ± 7	8.8 ± 5.3
Pd(DMP)	0.58	19 ± 4	2.7 ± 0.3
H_2DMP	0.54	55 ± 3	4.6 ± 1.4
Ni(DMP)	0.54	133 ± 27	8.6 ± 2.6
Cu(DMP)	0.46	118 ± 26	19.0 ± 8.7
Zn(DMP)	0.40	344 ± 51	41.0 ± 2.0
Co(DMP)	0.30[a]	424 ± 53	20.7 ± 14.5

[a] Irreversible.

Film Formation by oCVD and Film Characterization

The films were prepared in a custom-built oCVD reactor (Supporting Information, Scheme S1). To ensure a sufficient coupling efficiency in the oCVD experiments, the oxidant $FeCl_3$ was sublimed in ca. 20–28 fold excess with respect to the porphyrin monomers (Supporting Information, Table S1). The oCVD reaction of M(DMP) and $FeCl_3$ yields macroscopically homogeneous thin films on glass slides within 30 minutes.

Helium ion microscopy (HIM) of the resulting oCVD films confirms the formation of smooth and uniform thin films covering the whole surface of the substrates (Supporting Information, Figure S3). Iron chloride particles are present on the surface of the oCVD films as reported previously.[22] The films prepared by oCVD show a more uniform surface as compared to the reference films obtained by sublimation of M(DMP) as evidenced by HIM that is very suitable for topographic imaging due to its excellent surface sensitivity and high depth of field (Supporting Information, Figures S3–S4). The low roughness of the oCVD films is confirmed by AFM measurements (Supporting Information, Figure S5), revealing a roughness between 2.7 and 20.7 nm depending on the starting porphyrin (Table 1).

Although similar amounts of porphyrin evaporated during the oCVD process in all cases, the thickness of the different oCVD films differs significantly (Table 1). Particularly, the oCVD films obtained from H_2DMP, Pd(DMP) and FeCl(DMP) are much thinner (*d* = 19–55 nm), while the thickness of oCVD films obtained from Co(DMP) and Zn(DMP) reaches several hundreds of nanometers (Table 1). Interestingly, thickness and roughness of the films correlate inversely with the oxidation potentials of the monomers (Table 1; Supporting Information, Figures S6 and S7). A lower oxidation potential increases the film thickness likely due to facilitated oxidative coupling reactions of the mono-

Full Paper
doi.org/10.1002/ejic.202000243

mers. Gleason et al. reported that the gaseous by-product HCl released during the C-C coupling of 3,4-ethylenedioxythiophene employing $CuCl_2$ forms bubbles which affect the film roughness.[33] Consequently, fast and efficient coupling leads to larger bubbles and a larger roughness. These arguments support the observed correlation of film roughness and thickness with the oxidation potential of the monomer.

The film colors range from orange/dark green (M = Co, Ni, Cu, Zn and Pd), to light green (M = 2H, FeCl). The drastic color difference between the oCVD films and their respective reference films obtained by sublimation support the occurrence of reactions at the porphyrin macrocycle. The following sections analyze and discuss these gas phase reactions under oxidative conditions.

Dehydrogenative Coupling of Porphyrins

UV/Vis/NIR spectra of the thin films on glass substrates reveal broadened Q bands and significant absorption in the NIR spectral region for the oCVD films prepared from Co, Ni, Cu, Zn and Pd porphyrins (Figure 1a–e). This enhanced absorption points towards the formation of porphyrin tapes for all these metalloporphyrins. In contrast, films obtained from FeCl(DMP) and H_2DMP exhibit only very weak absorptions in the NIR spectral region (Figure 1f) suggesting less efficient oxidative coupling reactions.

Tsuda et al. reported that doubly linked Ni^{II} porphyrin tapes (Scheme 1; M = Ni; Ar = 3,5-di-*tert*-butylphenyl) exhibit an effective conjugation length (ECL) with an absorption maximum around 1480 nm.[9] On the other hand, the ECL of triply linked zinc porphyrin tapes [Scheme 1; M = Zn; Ar = 2,4,6-tris(3,5-di-*tert*-butylphenoxy) phenyl and 3,5-dioctyloxyphenyl] is reported to shift the absorption onset above 2800 nm.[34] Consequently, the films prepared from Co(DMP), Cu(DMP) and Zn(DMP) with appreciable absorptions above 1500 nm consist of triply linked porphyrin tapes in a significant amount. On the other hand, films prepared by oCVD from Ni(DMP) contain both doubly and triply linked fragments[30] and hence their absorption in the NIR is lower (Figure 1b). Finally, films prepared by oCVD from Pd(DMP) are essentially transparent above 1500 nm. This suggests mainly doubly linked porphyrin tapes being present in the Pd(DMP) derived film.

LDI-HR mass spectrometry of the films provides an insight into the reactivity of the different metalloporphyrins under oCVD. In fact, peaks corresponding to monomeric (n = 1) and oligomeric species (n = 2–6) are observed in the mass spectra (Figure 2 and Figure 3; Supporting Information, Figure S8). Chlorination with Cl_2 formed by decomposition of $FeCl_3$[35] yields oligochlorinated species ($\Delta m/z$ = 35).[36] Furthermore, the (simulated) isotopic pattern of (non-chlorinated) dimeric species (n = 2) reveals the number of linkages, namely from peaks corresponding to doubly linked cations $[M_2(DMP)_2–4H]^+$ and triply linked cations $[M_2(DMP)_2–6H]^+$ (Supporting Information, Figures S9–S11).

The LDI-HR spectra of films prepared by oCVD of H_2DMP show only monomeric species derived from chlorination and protonation (Figure 2).

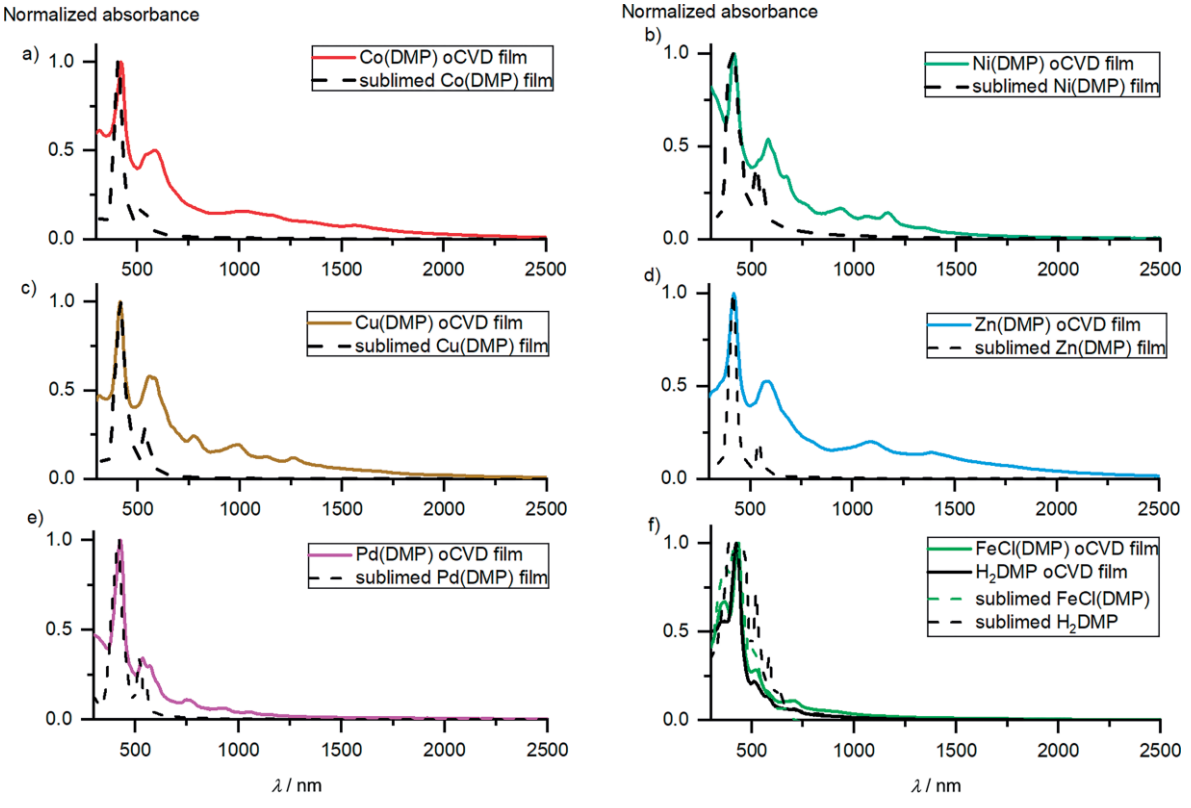

Figure 1. Normalized UV/Vis/NIR absorption spectra of the oCVD films and their respective reference films obtained from M(DMP) monomers.

Full Paper
doi.org/10.1002/ejic.202000243

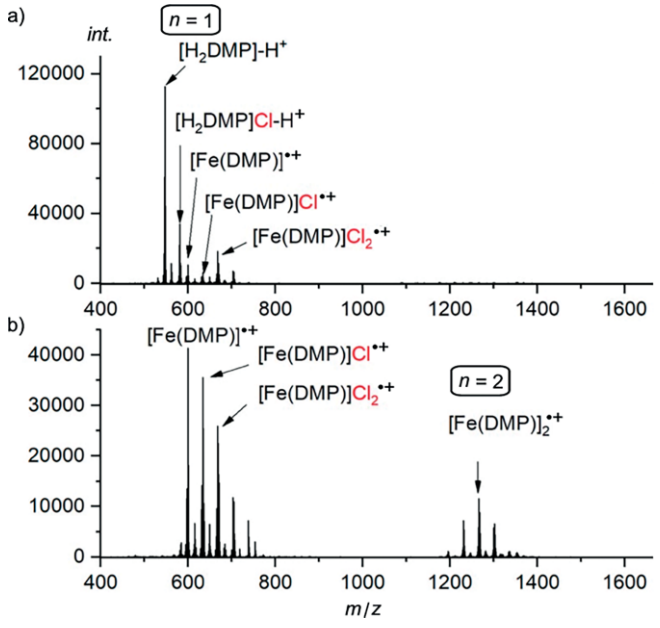

Figure 2. LDI-HRMS of oCVD films prepared from a) H_2DMP and b) FeCl(DMP) (n = degree of oligomerization).

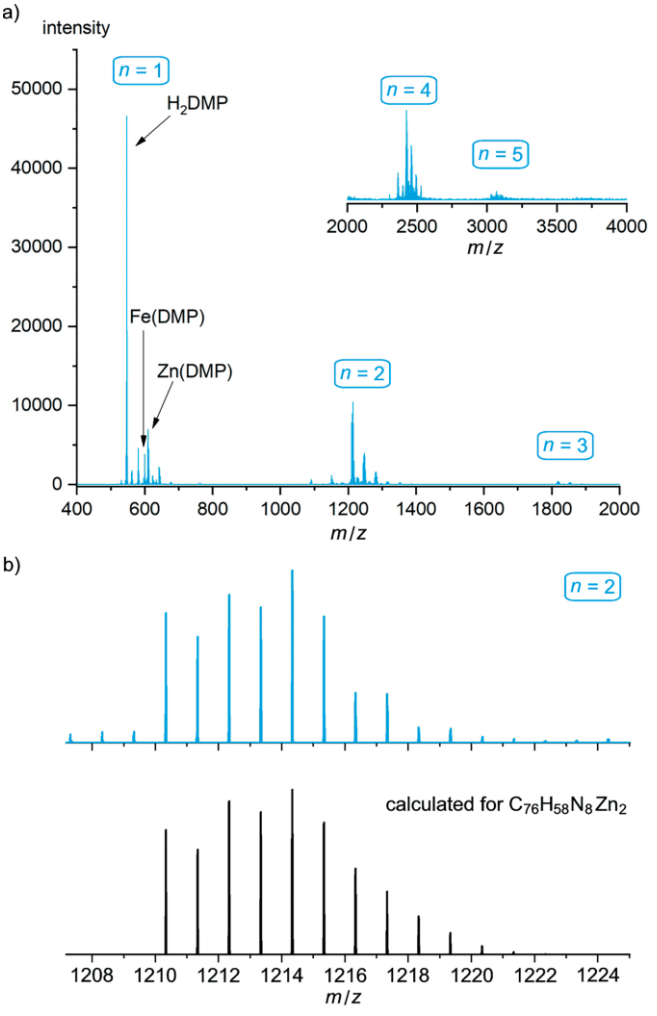

Figure 3. (a) LDI-HR mass spectra of the oCVD film prepared from Zn(DMP) in the 400–2000 and 2000–4000 m/z ranges (n = degree of oligomerization). The two spectra were acquired in separate scanning events. Peaks in the n = 1 region indicate demetalation of Zn(DMP) forming H_2DMP and the insertion of iron forming Fe(DMP) from the oxidant. (b) LDI-HR mass spectrum of the oCVD film prepared from Zn(DMP) in the dimer region (n = 2; blue) and the simulated spectrum (black) of the triply linked dimer $[Zn(DMP)]_2$–6H (calculated for $C_{76}H_{58}N_8Zn_2$).

Furthermore, iron-containing species are present as well. Obviously, C-C coupling is inefficient, while chlorination, protonation and iron insertion occur. The inefficient coupling of H_2DMP might be ascribed to the rather high oxidation potential of H_2DMP (Table 1) and the ease of its protonation to $[H_3DMP]^+$ (Figure 2a) and $[H_4DMP]^{2+}$, respectively, which further increases the oxidation potential of the monomer. A single peak in the N1s region of the XPS spectrum confirms the absence of free-base porphyrins (E = 400.4 and 398.4 eV) and suggests that only symmetric $[H_4DMP]^{2+}$ and $[Fe(DMP)]^+$ species (E = 399.1 eV) are present in this film (Supporting Information, Figures S12 and S13). This interpretation also agrees with the similar UV/Vis/NIR absorption spectra of films prepared by oCVD of H_2DMP and FeCl(DMP) (Figure 1).

The mass spectrum of the film derived from FeCl(DMP) shows peaks of monomers and dimers but only insignificant amounts of higher oligomers (Figure 2b). The simulation of the isotopic pattern of the dimer yields both double and triple linkages (Supporting Information, Figure S9a). The high oxidation potential of FeCl(DMP) and the loss of coordinated chloride yielding difficult-to-oxidize $[Fe(DMP)]^+$ can account for the poor degree of polymerization of FeCl(DMP) (Table 1). Furthermore, the flexible charge and spin localization in the oxidized complex, namely $[Fe^{III}Cl(DMP^{\bullet})]^+$ and $[Fe^{IV}(DMP)]^+$ could reduce the C-C coupling efficiency (vide infra).

The LDI-HRMS spectrum of films prepared by oCVD from Pd(DMP) exhibits signals pertaining to dimers, trimers, tetramers and pentamers confirming oligomerization process. The isotopic pattern of the (chlorine-free) dimer matches the pattern calculated for $[Pd_2(DMP)_2–4H]^+$. Consequently, the porphyrins are exclusively doubly linked (Supporting Information, Figures S8 and S10).

LDI-HRMS spectra of films prepared from Co(DMP), Ni(DMP) and Cu(DMP) display signals corresponding to oligomers as well (Supporting Information, Figure S8). However, simulation of the isotopic pattern of (chlorine-free) dimers suggests the presence of doubly and triply linked dimers $[M_2(DMP)_2–4H]^+$ and $[M_2(DMP)_2–6H]^+$ (M = Co, Ni, Cu) (Supporting Information, Figure S9).

Finally, LDI-HRMS spectra of the Zn(DMP) oCVD film exhibit signals of oligomeric species up to the pentamer (Figure 3a). Simulation of the isotopic pattern of the (chlorine-free) dimer confirms the exclusive presence of triply linked dimers $[Zn_2(DMP)_2–6H]^+$ only (Figure 3b, Supporting Information, Figure S11).

Zinc porphyrins demetallate in the presence of acids and formation of the free-base porphyrin H_2DMP is also confirmed for the films prepared by oCVD (Figure 3a). The intensity of the free-base porphyrin signal is, however, not comparable to the intensity of the Zn(DMP) signal due to the different charging

processes (protonation vs. ionization) and hence the relative amount of demetallation is undetermined. The mass spectrum furthermore shows a weak signal for Fe(DMP). The iron insertion (after demetallation) is similar to the reactivity of H_2DMP in the oCVD process with $FeCl_3$ (Figure 2a). Analogous peaks for iron-containing species are observed in the *m/z* ranges of oligomers.

The XPS spectrum of the Zn(DMP) oCVD film shows broadened Zn2p and N1s peaks and a new N1s peak at higher binding energy (400.3 eV). The latter is assigned to the nitrogen atoms of the free-base porphyrin (Supporting Information, Figure S14). XPS analysis thus supports the partial demetalation of Zn(DMP) under oCVD conditions.

Regioselectivity of the Initial C-C Bond Formation

The generally accepted reaction mechanism of the oxidative C-C coupling reaction between porphyrins starts with a nucleophilic attack of a neutral porphyrin at a porphyrin radical cation.[6,7,10,19,31]

In most cases, the porphyrin's *meso* position is the most electron-rich nucleophilic site. Consequently, the porphyrin radical cation coupling partner dictates the regioselectivity of the first C-C bond formation (*meso-meso* or *meso-β*; Scheme 2). The symmetry of the SOMO of the radical cation is either a_{1u} with large orbital coefficients at the β positions or a_{2u} with large orbital coefficients at the *meso* positions (Scheme 2).[37]

The prediction of the oxidation product of metalloporphyrins is not trivial, highly debated in literature and depends on the nature of the metal cation, the porphyrin substituents, the axial ligands and the physical state (solution, gas or solid).[38–43] With redox active metal cations the oxidation of the metal center itself can occur.[40–42,44]

Zinc diphenyl porphyrin radical cations host the unpaired electron in the porphyrin's π orbital of a_{2u} symmetry.[8] This fits to the observed regioselective *meso-meso* and triply linked porphyrins (Scheme 2). Contrarily, the SOMO of palladium diphenyl porphyrin radical cations possesses a_{1u} symmetry.[6,45] This description agrees with the observed regioselective *meso-β* and doubly linked porphyrins (Scheme 2).[6,7]

Based on resonance Raman spectroscopy, Spiro and co-workers suggested that Cu^{II}(TPP), Ni^{II}(TPP) and Fe^{III}Cl(TPP) (H_2TPP = *meso*-tetraphenyl porphyrin) are subject to pseudo-Jahn–Teller distortions upon oxidation.[41] The distortion lowers the symmetry yielding mixed a_{1u}/a_{2u} radical cation character.[40] Indeed, Ni^{II} diphenyl porphyrins form double and triple linkages under oCVD conditions.[31] A similar effect might be operative in copper(II) and iron(III) diphenyl porphyrins since both solution based[11,12,45] and the present oCVD experiments yield doubly and triply-linked copper(II) porphyrin tapes.

Consequently, the electron configuration and the electron donating character of the central metal ion determine the regioselectivity of the connectivity via the SOMO symmetry of the porphyrin (Scheme 2).

Interplay with Metal Centered Oxidation: Co(DMP) and FeCl(DMP)

Metal-centered oxidations can compete with the porphyrin oxidation, especially with cobalt(II) and iron(III) as central ions.

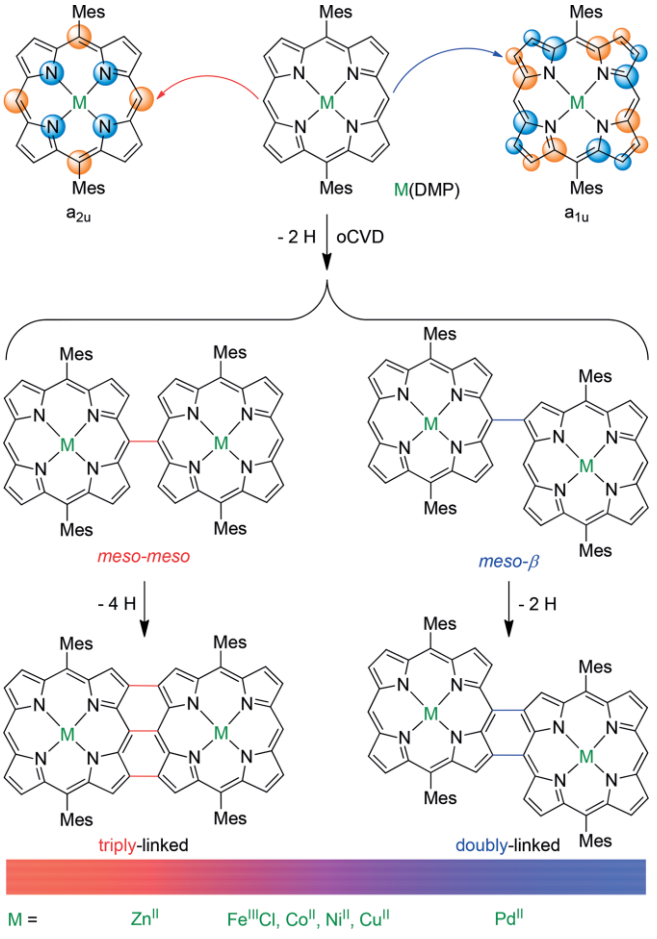

Scheme 2. Effect of the metal center in the initial C-C bond forming step during the oCVD process of metalloporphyrins. The a_{2u}/a_{1u} symmetry[37] of the SOMO of porphyrins is indicated with blue and orange spheres.

Indeed, Kadish, Sankar et al. recently observed an equilibrium between the cobalt(III) porphyrin and the cobalt(II) porphyrin radical cation in non-coordinating solvents.[44] Similar observations have been reported for iron(III) porphyrins depending on the porphyrin's substituents and the axial ligands on iron.[42,46]

Compared to sublimed Co^{II}(DMP) with only cobalt(II) being present, the Co2p XPS peak of the film prepared from Co(DMP) by oCVD is broadened and shifted from 780.9 to 781.7 eV towards higher binding energy (Supporting Information, Figure S15). We ascribe these peaks to the presence of both Co^{II} and Co^{III} porphyrins supporting the valence isomeric nature of the $[Co(DMP)]^+$, namely $[Co^{III}(DMP)]^+$ and $[Co^{II}(DMP^{\bullet})]^+$. In addition, the N1s XPS signal exhibits a new contribution at higher binding energy confirming the presence of nitrogen atoms with increased positive charge (Supporting Information, Figure S15). In the gas phase, both $[Co^{III}(DMP)]^+$ and $[Co^{II}(DMP^{\bullet})]^+$ valence isomers could be present. As the Co(DMP) derived film contains high oligomers, the reactive $[Co^{II}(DMP^{\bullet})]^+$ π radical valence isomer appears to be prevalent during deposition enabling the oligomerization process.

A similar valence isomeric equilibrium could be established by iron porphyrins, i.e. $[Fe^{IV}Cl(DMP)]^+$ and $[Fe^{III}Cl(DMP^{\bullet})]^+$. However, XPS analysis in the iron region was of little help due to

Full Paper
doi.org/10.1002/ejic.202000243

the contamination with the iron chloride oxidant. A dominant $[Fe^{IV}Cl(DMP)]^+$ valence isomer would disfavor the oligomerization and could be one reason for the poor oligomerization yield of FeCl(DMP) in addition to its high redox potential (Table 1).

Electrical Conductivity of the Films

To assess the conductivity of the oCVD films independently from insulating oxidant inclusions (Supporting Information, Figure S16), conductive atomic force microscopy (C-AFM) was employed to evaluate the local electron-current distribution, i.e. the local conductivity without the perturbation of the oxidant inclusions. C-AFM measurements of the films obtained from M(DMP) via oCVD reveal a striking influence of the metal center (Figure 4, Supporting Information, Figure S17).

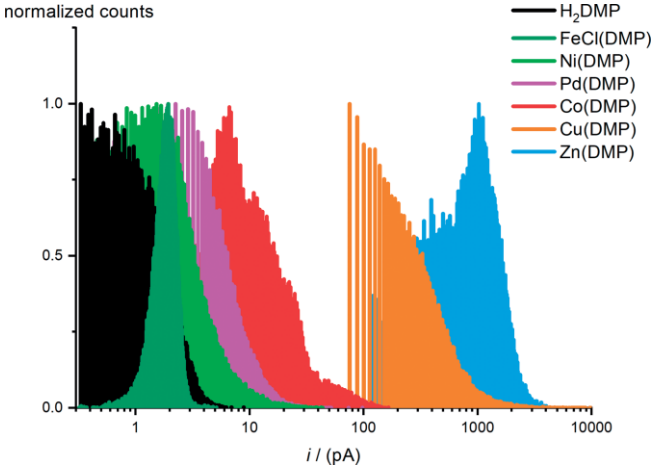

Figure 4. Histograms of the current obtained from the C-AFM measurements (logarithmic scale). Cu(DMP) and Zn(DMP) exhibit the highest currents in the series.

Clearly, films prepared from H_2DMP and FeCl(DMP) by oCVD display the lowest conductivity. This is expected based on the very poor polymerization observed by LDI-HRMS and the absent NIR absorption.

The excellent conductivity of the Zn(DMP) oCVD film (Figure 4; Supporting Information, Figure S17) likely arises from the exclusive triple linkages in the porphyrin tapes,[4,5,47,48] the good polymerization yield (LDI-HRMS, UV/Vis/NIR) and the absence of redox active metal centers and strongly bound axial ligands.

The film prepared from Cu(DMP) by oCVD displays a high conductivity as well, yet lower than that of the zinc porphyrin thin film. The presence of some double linkages instead of triple linkages could account for this behavior.

The cobalt porphyrin derived thin film possessing both triple and double linkages is significantly less conductive, likely because of the presence of cobalt(III) centers (vide supra). Cobalt(III) strongly coordinates axial ligands (e.g. chloride or water).[49] This increases the distance between the tapes in the film aggravating electron tunneling between tapes. Furthermore, cobalt(III) centers could act as electron traps diminishing the conductivity.

The films prepared by oCVD from the d^8 metalloporphyrins Ni(DMP) and Pd(DMP) are even less conductive. The poor conductivity of the palladium containing film probably results from the dominant double linkages and that of the Ni(DMP) derived film due to a poor ratio of triple:double linkages and possible axial ligands at the nickel(II) center.

Conclusion

Thin films of multiply linked porphyrin tapes were prepared via oxidative chemical vapor deposition of M(DMP) {M = Co^{II}, Ni^{II}, Cu^{II}, Zn^{II} and Pd^{II}; DMP = 5,15-(dimesityl)porphyrinato} and $FeCl_3$ as oxidant. Free-base porphyrins and iron(III) porphyrins failed to give polymers. The central metal ion affects the regioselectivity of the of the C–C coupling reaction. Zn(DMP) yields triply-linked and Pd(DMP) doubly-linked porphyrin tapes, while Co(DMP), Ni(DMP) and Cu(DMP) give porphyrin tapes with mixed connectivity. The different regioselectivity relates to the symmetry of the SOMO of the radical cation. The linkage of the porphyrins, the axial ligation of the metal center and the redox activity of the metal affect the electrical conductivity of the metalloporphyrin films. Zinc(II) and copper(II) porphyrin tapes deliver the highest conductivity along with an appreciable NIR absorbance up to 2000 nm.

Experimental Section

Materials: 5,15-(Dimesityl) metalloporphyrins were obtained from PorphyChem and used without further purification (98 %). Iron(III) chloride (97 %) was obtained from Sigma-Aldrich and used without further purification. Dichloromethane used for cyclic voltammetry experiments was dried with CaH_2 and distilled prior to use.

Methods: Thermogravimetric analyses were performed with a TGA 2 from Mettler Toledo equipped with XP1U balance under argon atmosphere with a ramp of 10 K min^{-1}. Cyclic voltammetric measurements were carried out with a BioLogic SP-50 voltammetric potentiostat. The porphyrins were dissolved (1 mM) in CH_2Cl_2 containing 0.1 M $[nBu_4N][PF_6]$ as supporting electrolyte. A platinum working electrode, a platinum wire counter electrode and a 0.01 M $Ag/AgNO_3$ reference electrode were used for the experiments. Cyclic voltammograms were recorded at 100 mV s^{-1} scan rate. Ferrocene was employed as internal reference redox system. All measurements were performed under an inert atmosphere in a glove box. The optical absorbance of the films was measured in the range of 250–2500 nm with a UV/Vis/NIR spectrophotometer (PerkinElmer, Lambda 950) with a 150 mm-diameter integrating sphere. The absorption spectra were recorded directly on the glass substrates. The thin films thicknesses were measured using a KLA-Tencor P-17 Stylus profiler. Images of the topography and conductivity of the samples were simultaneously acquired using the C-AFM mode of an Innova AFM (Bruker). Conductive AFM tips ElectriMulti75-G from BudgetSensors coated with a layer of 5 nm chromium and 25 nm of platinum with nominal spring constants of 3 N m^{-1} and nominal radius <25 nm were used. Images of a 2 × 2 μm^2 area with a resolution of 256 × 256 pixels were taken at a scan rate of 0.5 Hz. Samples were deposited on monocrystalline silicon wafers coated with platinum and connected to the conductive stage via a silver colloidal ink. The topography was obtained by maintaining the tip deflection constant (0.25 V) via the feedback loop of the AFM acting on the

piezo Z direction. A bias of +4 V was applied to the back electrode of the samples while the grounded conductive tip was collecting electrons for the current measured by an amplifier (DLPCA-200, Femto). A 109 V A^{-1} amplification was used for the pA current range and a 107 V A^{-1} for the ones in nA range and the signal output was then transmitted to the AFM electronics and recorded. The reported average and standard deviation values of conductivity and roughness (*Ra*) consider at least four images in each sample for reliable results. Noise on current detection is appearing at low values, this is close to the limit of noise of the amplifier. A 80 nm wavelength filter is applied before to remove this noise prior to roughness measurement. HIM images were acquired with a ZEISS ORION Nanofab Helium Ion Microscope (HIM). Contrast is essentially due to topography and composition of the sample. He^+ or Ne^+ ions are produced in the Gas Field Ionization Source (GFIS). The upper part of the instrument contains a tungsten filament. Its tip consists only of three atoms (trimer) and is set under a positive high voltage with respect to the extraction electrode and cryo-cooled simultaneously. Surrounded by He or Ne gas atoms these become ionized at the tip apex and are accelerated in this case with 30 keV towards the sample. The trimer is emitting three beamlets whereas one atom is selected as the main emitter. While raster scanning over the surface secondary electrons (SE) are produced by impacting He^+ or Ne^+ primary ions and are detected by an Everhart-Thornley detector. A spatial resolution of down to 0.5 nm is achievable with HIM. Advantages compared to a regular scanning electron microscope (SEM) are the high surface sensitivity and large depth of field favouring topographic imaging.[50,51] Compared to standard secondary electron microscope (SEM), HIM allows to probe surfaces with a better sensitivity and a higher depth of field, which makes HIM very suitable for topographic imaging.[50,51] For this set of images, the primary ion current was varying between 0.1 and 0.6 pA. The working distance was at around 17 mm. Since a prototype instrument was used, higher sample stage positions and therefore smaller working distances were not feasible in the current prototype setup. Atmospheric-pressure LDI-HRMS was employed for characterisation of the coatings. HRMS analyses were performed with an LTQ/Orbitrap Elite Hybrid Linear Ion Trap-Orbitrap Mass Spectrometer from Thermo Scientific (San Jose, CA) coupled with an AP-LDI (ng) UHR source from MassTech Inc (Columbia, MA) with a 355 nm Nd:YAG laser. The thin films were directly probed without any matrix deposition by the laser following a spiral motion during 30 s per sample. An in-source decay (ISD) of 70 V was applied to the samples in order to prevent any formation of non-covalent porphyrin clusters that could interfere with the distribution of the oligomers. A maximum injection time of 800 ms and a resolving power of 240000 at *m/z* 400 in the normal mass range (*m/z* 300–2000) and the high mass range (*m/z* 1800–4000) were employed for the HRMS analyses.

Preparation of the Films: The films were prepared in a custom-built oCVD reactor (Supporting Information, Scheme S1). The two evaporators, located at the bottom of the reaction chamber, were loaded with porphyrins (10 mg) and $FeCl_3$ (150 mg), respectively. Microscope glass slides and silicon wafers were used as substrates. Argon (Air Liquide, 99.999 %) is introduced in the chamber to tune the pressure inside the chamber (10^{-3} mbar). The substrate holder is heated at 100 °C to facilitate the reaction. The deposition time was 30 minutes in all experiments. Reference coatings were obtained under the same conditions (substrate temperature of 100 °C and pressure of 10^{-3} mbar) without supplying oxidant. Further details are given in Table S1 (Supporting Information).

Acknowledgments

We gratefully acknowledge the financial support of the Luxembourg National Research Fund (http://fnr.lu) through the POLYPORPH project (C15/MS/10340560/POLYPORH/ Boscher). D. El Assad, Dr. G. Frache, and Dr. J. Guillot from LIST are acknowledged for insightful discussions and acquisition of the mass and XPS spectra.

Keywords: Chemical vapor deposition · Porphyrins · Thin films · Oxidative coupling · Metalloporphyrins

[1] A. Tsuda, A. Osuka, *Science* **2001**, *293*, 79–82.
[2] M. O. Senge, M. Fazekas, E. G. A. Notaras, W. J. Blau, M. Zawadzka, O. B. Locos, E. M. Ni Mhuircheartaigh, *Adv. Mater.* **2007**, *19*, 2737–2774.
[3] H. S. Cho, D. H. Jeong, S. Cho, D. Kim, Y. Matsuzaki, K. Tanaka, A. Tsuda, A. Osuka, *J. Am. Chem. Soc.* **2002**, *124*, 14642–14654.
[4] a) E. Leary, B. Limburg, A. Alanazy, S. Sangtarash, I. Grace, K. Swada, L. J. Esdaile, M. Noori, M. T. González, G. Rubio-Bollinger, H. Sadeghi, A. Hodgson, N. Agraït, S. J. Higgins, C. J. Lambert, H. L. Anderson, R. J. Nichols, *J. Am. Chem. Soc.* **2018**, *140*, 12877–12883; b) G. Sedghi, L. J. Esdaile, H. L. Anderson, S. Martin, D. Bethell, S. J. Higgins, R. J. Nichols, *Adv. Mater.* **2012**, *24*, 653–657.
[5] a) P. Gao, Z. Chen, Z. Zhao-Karger, J. E. Mueller, C. Jung, S. Klyatskaya, T. Diemant, O. Fuhr, T. Jacob, R. J. Behm, M. Ruben, M. Fichtner, *Angew. Chem. Int. Ed.* **2017**, *56*, 10341–10346; *Angew. Chem.* **2017**, *129*, 10477–10482; b) Z. Chen, P. Gao, W. Wang, S. Klyatskaya, Z. Zhao-Karger, D. Wang, C. Kebel, O. Fuhr, M. Fichtner, M. Ruben, *ChemSusChem* **2019**, *12*, 3737–3741; c) L. Xie, X. Li, B. Wang, J. Meng, H. Lei, W. Zhang, R. Cao, *Angew. Chem. Int. Ed.* **2019**, *58*, 18883–18887; *Angew. Chem.* **2019**, *131*, 19059–19063.
[6] Y. Nakamura, N. Aratani, A. Tsuda, A. Osuka, K. Furukawa, T. Kato, *J. Porphyrins Phthalocyanines* **2003**, *7*, 264–269.
[7] C.-M. Feng, Y.-Z. Zhu, S.-C. Zhang, Y. Zang, J.-Y. Zheng, *Org. Biomol. Chem.* **2015**, *13*, 2566–2569.
[8] N. Aratani, A. Osuka, *Chem. Rec.* **2003**, *3*, 225–234.
[9] A. Tsuda, Y. Nakamura, A. Osuka, *Chem. Commun.* **2003**, 1096–1097.
[10] A. Tsuda, A. Nakano, H. Furuta, H. Yamochi, A. Osuka, *Angew. Chem. Int. Ed.* **2000**, *39*, 558–561; *Angew. Chem.* **2000**, *112*, 572–575.
[11] B. J. Brennan, M. J. Kenney, P. A. Liddell, B. R. Cherry, J. Li, A. L. Moore, T. A. Moore, D. Gust, *Chem. Commun.* **2011**, *47*, 10034–10036.
[12] B. J. Brennan, J. Arero, P. A. Liddell, T. A. Moore, A. L. Moore, D. Gust, *J. Porphyrins Phthalocyanines* **2013**, *17*, 247–251.
[13] D. Y. Kim, T. K. Ahn, J. H. Kwon, D. Kim, T. Ikeue, N. Aratani, A. Osuka, M. Shigeiwa, S. Maeda, *J. Phys. Chem. A* **2005**, *109*, 2996–2999.
[14] K. Rybicka-Jasińska, W. Shan, K. Zawada, K. M. Kadish, D. Gryko, *J. Am. Chem. Soc.* **2016**, *138*, 15451–15458.
[15] D. Khusnutdinova, B. L. Wadsworth, M. Flores, A. M. Beiler, E. A. Reyes Cruz, Y. Zenkov, G. F. Moore, *ACS Catal.* **2018**, *8*, 9888–9898.
[16] E. Rose, B. Andrioletti, S. Zrig, M. Quelquejeu-Ethève, *Chem. Soc. Rev.* **2005**, *34*, 573–583.
[17] S. Lin, C. S. Diercks, Y.-B. Zhang, N. Kornienko, E. M. Nichols, Y. Zhao, A. R. Paris, D. Kim, P. Yang, O. M. Yaghi, C. J. Chang, *Science* **2015**, *349*, 1208–1213.
[18] S. Preiß, A. Päpcke, L. Burkhardt, L. Großmann, S. Lochbrunner, M. Bauer, T. Opatz, K. Heinze, *Chem. Eur. J.* **2019**, *25*, 5940–5949.
[19] A. Osuka, H. Shimidzu, *Angew. Chem. Int. Ed. Engl.* **1997**, *36*, 135–137; *Angew. Chem.* **1997**, *109*, 93–95.
[20] N. Yoshida, N. Aratani, A. Osuka, *Chem. Commun.* **2000**, 197–198.
[21] K. Sugiura, T. Matsumoto, S. Ohkouchi, Y. Naitoh, T. Kawai, Y. Takai, K. Ushiroda, Y. Sakata, *Chem. Commun.* **1999**, 1957–1958. .
[22] K. Baba, G. Bengasi, D. El Assad, P. Grysan, E. Lentzen, K. Heinze, G. Frache, N. D. Boscher, *Eur. J. Org. Chem.* **2019**, 2368–2375.
[23] G. Bengasi, K. Baba, G. Frache, J. Desport, P. Gratia, K. Heinze, N. D. Boscher, *Angew. Chem. Int. Ed.* **2019**, *58*, 2103–2108; *Angew. Chem.* **2019**, *131*, 2125–2130.

[24] L. M. Mateo, Q. Sun, S. Liu, J. J. Bergkamp, K. Eimre, C. A. Pignedoli, P. Ruffieux, S. Decurtins, G. Bottari, R. Fasel, T. Torres, *Angew. Chem. Int. Ed.* **2020**, *59*, 1334–1339; *Angew. Chem.* **2020**, *132*, 1350–1355.
[25] A. Wiengarten, K. Seufert, W. Auwärter, D. Ecija, K. Diller, F. Allegretti, F. Bischoff, S. Fischer, D. A. Duncan, A. C. Papageorgiou, F. Klappenberger, R. G. Acres, T. H. Ngo, J. V. Barth, *J. Am. Chem. Soc.* **2014**, *136*, 9346–9354.
[26] B. Cirera, B. De La Torre, D. Moreno, M. Ondráček, R. Zbořil, R. Miranda, P. Jelínek, D. Écija, *Chem. Mater.* **2019**, *31*, 3248–3256.
[27] Y. He, M. Garnica, F. Bischoff, J. Ducke, M. Bocquet, M. Batzill, W. Auwärter, J. V. Barth, *Nat. Chem.* **2017**, *9*, 33–38.
[28] J. P. Lock, S. G. Im, K. K. Gleason, *Macromolecules* **2006**, *39*, 5326–5329.
[29] M. Heydari Gharahcheshmeh, K. K. Gleason, *Adv. Mater. Interfaces* **2019**, *6*, 1801564.
[30] G. Bengasi, J. S. Desport, K. Baba, J. P. Cosas Fernandes, O. De Castro, K. Heinze, N. D. Boscher, *RSC Adv.* **2020**, *10*, 7048–7057.
[31] G. Bengasi, K. Baba, O. Back, G. Frache, K. Heinze, N. D. Boscher, *Chem. Eur. J.* **2019**, *25*, 8313–8320.
[32] M. Grzybowski, B. Sadowski, H. Butenschön, D. Gryko, *Angew. Chem. Int. Ed.* **2020**, *59*, 2998–3027; *Angew. Chem.* **2020**, *132*, 3020–3050.
[33] S. G. Im, D. Kusters, W. Choi, S. H. Baxamusa, M. C. M. van de Sanden, K. K. Gleason, *ACS Nano* **2008**, *2*, 1959–1967.
[34] T. Ikeda, N. Aratani, A. Osuka, *Chem. Asian J.* **2009**, *4*, 1248–1256.
[35] M. W. Chase Jr., C. A. Davies, J. R. Downey Jr., D. J. Frurip, R. A. McDonald, A. N. Syverud, *J. Phys. Chem. Ref. Data* **1985**, *14*, 903.
[36] T. Wijesekera, A. Matsumoto, D. Dolphin, D. Lexa, *Angew. Chem. Int. Ed. Engl.* **1990**, *29*, 1028–1030; *Angew. Chem.* **1990**, *102*, 1073–1074.
[37] M. Gouterman, *J. Mol. Spectrosc.* **1961**, *6*, 138–163.
[38] A. Wolberg, J. Manassen, *Inorg. Chem.* **1970**, *9*, 2365–2367.
[39] D. Chatterjee, E. Balasubramanian, *J. Coord. Chem.* **1999**, *46*, 467–470.
[40] J. Seth, V. Palaniappan, D. F. Bocian, *Inorg. Chem.* **1995**, *34*, 2201–2206.
[41] R. S. Czernuszewicz, K. A. Macor, X. Y. Li, J. R. Kincaid, T. G. Spiro, *J. Am. Chem. Soc.* **1989**, *111*, 3860–3869.
[42] A. Ikezaki, M. Takahashi, M. Nakamura, *Chem. Commun.* **2013**, *49*, 3098–3100.
[43] W. F. Scholz, C. A. Reed, Y. J. Lee, W. R. Scheidt, G. Lang, *J. Am. Chem. Soc.* **1982**, *104*, 6791–6793.
[44] X. Ke, R. Kumar, M. Sankar, K. M. Kadish, *Inorg. Chem.* **2018**, *57*, 1490–1503.
[45] M. Kamo, A. Tsuda, Y. Nakamura, N. Aratani, K. Furukawa, T. Kato, A. Osuka, *Org. Lett.* **2003**, *5*, 2079–2082.
[46] G. Buisson, A. Deronzier, E. Duee, P. Gans, J. C. Marchon, J. R. Regnard, *J. Am. Chem. Soc.* **1982**, *104*, 6793–6796.
[47] N. Algethami, H. Sadeghi, S. Sangtarash, C. J. Lambert, *Nano Lett.* **2018**, *18*, 4482–4486.
[48] D. H. Yoon, S. B. Lee, K. H. Yoo, J. Kim, J. K. Lim, N. Aratani, A. Tsuda, A. Osuka, D. Kim, *J. Am. Chem. Soc.* **2003**, *125*, 11062–11064.
[49] K. M. Kadish, K. M. Smith, R. Guilard, *The Porphyrin Handbook: Inorganic, Organometallic and Coordination Chemistry*, Academic Press, **2003**.
[50] T. Wirtz, O. De Castro, J.-N. Audinot, P. Philipp, *Annu. Rev. Anal. Chem.* **2019**, *12*, 523–543.
[51] *Helium Ion Microscopy* (Eds.: G. Hlawacek, A. Gölzhäuser), Springer International Publishing, **2016**.

Received: March 6, 2020